Enhancing photon collection from single shallow nitrogen-vacancy centers in diamond nanopillars for quantum heterodyne measurements

Akirabha Chanuntranont [1*], Kazuki Otani [1], Daiki Saito [1], Yuki Ueda [1], Masato Tsugawa [1], Shuntaro Usui [1], Yuto Miyake [1], Tokuyuki Teraji [2], Shinobu Onoda [3], Takahiro Shinada [4], Hiroshi Kawarada [1], Takashi Tanii [1†]

[1] School of Fundamental Science and Engineering, Waseda University, 3-4-1 Okubo, Shinjuku, Tokyo 169-8555, Japan

[2] National Institute for Materials Science, 1-1 Namiki, Tsukuba, Ibaraki 304-0044, Japan

[3] National Institutes for Quantum Science and Technology, 1233 Watanuki, Takasaki, Gunma 370-1292, Japan

[4] Center for Innovative Integrated Electronic Systems, Tohoku University, 468-1 Aramaki-aza-aoba, Aoba, Sendai, Miyagi 980-8572, Japan

The developments in quantum sensing protocols and nano-photonic waveguides are merged to improve the performance of single nitrogen-vancancy (NV) centers in nuclear magnetic resonance (NMR) sensing. Nanopillars are designed with NV centers placed 5 nm below the top facet and fabricated through a simple procedure, suitable for mass production. Fluorescence intensities from these nanopillars are 3.5 times greater than that of single shallow NV centers embedded in unstructured flat diamond. Quantum heterodyne measurements of an alternating magnetic field are performed with these nanopillars and evidence of improved peak clarity in the frequency spectrum is shown.

Single nitrogen-vacancy (NV) centers in diamond are promising sensors for nanoscale nuclear magnetic resonance (NMR) measurements.[1–3] An electron trapped in a diamond NV center lends itself to optical spin state initialization, fluorescent spin state readout, and may be manipulated coherently even in ambient conditions.[4] Particularly, due to increased sensitivity from their close proximity to target spins, NV centers within 5 nm of the diamond surface (shallow NV centers) can be used to detect the alternating magnetic field (AMF) induced by nuclear spins placed on the diamond surface.[5–9] In general configurations, shallow diamond NV centers have a reported magnetic sensitivity in the order of $\sim 1\,\mu\mathrm{T}/\sqrt{\mathrm{Hz}\cdot\mu\mathrm{m}^{-2}}$.[10] This sensitivity allows the detection of single atomic nuclei such as ^{13}C, ^{1}H and ^{19}F placed on the diamond surface and is also suf-

*The first, second and third authors contributed equally to this work

†E-mail address: tanii@waseda.jp

ficient to measure the distance between the NV center and target nuclear spins with atomic-scale accuracy.[11,12]

While shallow single NV centers have proven to be highly sensitive in practice, two factors limit their usefulness as nano-NMR sensors. First, the frequency resolution of shallow NV centers remains limited. Typical AMF measurements with diamond NV centers achieve frequency resolutions in the kHz regime, while frequency resolutions below $10\,\mathrm{Hz}$ are required to identify the chemical structure around target nuclear spins by resolving chemical shifts and J-coupling.[12,13] In principle, higher frequency resolutions can be obtained by prolonging the measurement duration, which is limited by the coherence time of NV center electron spins. However, while electrons of NV centers located in bulk diamond demonstrate long coherence times at ambient conditions, coherence times are decreased considerably for shallow NV centers due to surface imperfections, such as dangling bonds and surface-modified phonons, in addition to paramagnetic sources such as ^{13}C and P1 centers in the diamond.[14–16]

The second limiting factor is the low photon collection efficiency caused by the high refractive index of diamond, which is approximately 2.42 at the air-diamond interface. From a single NV center near the surface of unstructured (flat) diamond, we achieve on average 40 kC/s. Once again, it is possible to compensate for the low photon collection by prolonging the measurement duration, but this would require an intractably long measurement duration and is not feasible considering the limited stability of our optical equipment. To obtain good NMR measurement results in tractable time, photon counts consistently above 100 kC/s are desired.

Potential solutions to these two problems have arisen in two independent strands of research. One strand of research is focused on the development of quantum sensing protocols. In this strand, multiple groups have developed a sensing protocol known as quantum heterodyne (qdyne) which claims to overcome the limitation in frequency resolution.[17–19] As the name suggests, the method adapts the conventional heterodyne method from signal processing to be used for quantum sensing with NV centers. In AMF measurements, the Larmor precession of the NV center electron spin is modulated in the presence of an AMF. In qdyne, this modulation is accumulated as a phase shift of the electron spin using an XY8-k pulse sequence.[20] Readout of the phase shift is obtained by pulsed optically detected magnetic resonance (ODMR), where changes in photon counts are expected to be proportional to the phase shift, hence the phase of the AMF. Photon detection is performed at regular time intervals and the obtained photon

count time series is processed by a fast Fourier transform (FFT). As a result, qdyne measurements produce peaks in the frequency regime at frequencies much lower than that of the AMF. Each peak is then mapped to the frequency of the applied AMF using the relationship between the two frequency regions. The reason that qdyne achieves a high frequency resolution is that the number of samples can be increased arbitrarily with a stable external clock, unrestricted by the coherence time of NV center electron spins.[17)]

A second strand of research is focused on the development of nano-photonic waveguides. These waveguides attempt to improve the photon collection efficiency from single NV centers in diamond by exploiting characteristics ranging from enhancements in mode couplings to optimization of the diamond surface to maximize critical angle approaches.[21–37)] However, this strand of research is primarily focused on improving the fluorescence characteristics of single NV centers in diamond with little regard to the requirements of NMR sensing, such as charge stability, NV center depth and frequency resolution.

In this paper, we merge these two strands of research and present results for an AMF measurement, relevant to nano-NMR sensing. We propose a nanopillar design optimized for a single NV center placed $5\,\mathrm{nm}$ below the diamond surface and present a simple method for fabricating these nanopillars, suitable for mass production. The photon counts and coherence time of NV center electron spins in these nanopillars are compared with those in flat diamond. Finally, we perform qdyne AMF measurements and compare the peak-to-floor-level fluctuation of the spectrum obtained from a single NV center in a nanopillar to that from flat diamond.

The nanopillar dimensions were optimized for a single NV center placed $5\,\mathrm{nm}$ below the diamond surface via a parameter grid-search using finite-difference time-domain (FDTD) simulations (OptiFDTD, Optiwave Systems). In these simulations, the diamond substrate is modelled after chemical-vapour-deposition (CVD) diamond, which is an isotropic crystal with a refractive index of $2.4151 + i9.096 \times 10^{-5}$. The NV center is simulated as a point source emitting a $637\,\mathrm{nm}$ continuous wave with an E_y component. The background mesh is simulated as air, with a refractive index of 1. As the control model, flat diamond is simulated as a diamond slab of $0.5\,\mu\mathrm{m}$ thickness and $3\,\mu\mathrm{m}$ width. The NV center is placed $5\,\mathrm{nm}$ below the diamond surface. The fluorescence power, in Watts, is measured as an area average at the end of the mesh $1\,\mu\mathrm{m}$ away from the diamond surface. For the grid search, the nanopillar is modelled as a perfect diamond

cylinder and we vary the cylinder diameter and length. The domain of the grid search is diameter $\in$ [10 nm, 300 nm] in steps of 10 nm and length $\in$ [50 nm, 600 nm] in steps of 50 nm. The nanopillars are placed on top of the previously described flat diamond substrate. For each nanopillar, the NV center is placed 5 nm below the nanopillar's top facet and the fluorescence power is measured as an area average at the end of the mesh 1 µm away from the top facet. For all simulations, the mesh parameters used are δx, δy, δz =0.01 µm each, with $\delta t = 1.66782047599076 \times 10^{-17}$ running for 30,000 timesteps. Anisotropic perfect matched layer (APML) boundary conditions were used.

An example of results from the FDTD simulations are shown in Fig. 1 (a) and (b) for an optimal nanopillar and flat diamond respectively. The optimal nanopillar has a width of 200 nm and a length of 400 nm. The total simulation volumes used to produce the results in Fig.1 (a) and (b) are x, y, z dimensions of 3 µm×3 µm×1.9 µm=17.1 µm^3 and 3 µm×3 µm×1.5 µm=13.5 µm^3 respectively. These results suggest that the fluorescence enhancement from nanopillars may be due to an optical cavity caused by differences between the optical modes of the nanopillar and bulk diamond. The presence of an optical cavity in the nanopillar can be seen in Fig. 1 (a) as light is reflected between the top and bottom of the pillar, leading to enhanced photon collection through the pillar apex. Meanwhile, Fig. 1 (b) shows that the air-diamond interface reflects most of the photons emitted by the NV center back to the diamond bulk in measurements with a flat diamond surface. In the optical cavity model, continued reflection between the pillar's top, air-diamond interface, and bottom, pillar-bulk interface, may induce an optical resonance that enhances photon collection at the air-diamond interface. However, further research will be necessary to further develop this model.

Nanopillars were fabricated on an approximately 20 µm thick, 99.95% ^{12}C-enriched homoepitaxial diamond film grown on a type-Ib high-pressure high-temperature (100) single-crystalline diamond substrate. An overview of the fabrication process is provided in Fig. 2 (a). The growth conditions for the high-quality homoepitaxial film are described elsewhere.[38,39] First, ^{15}N ions were implanted into the film at an acceleration energy of 2.5 keV with a fluence of 1.5×10^{11} cm^{-2}. After cleaning the diamond substrate with a hot mixed acid solution ($HNO_3 : H_2SO_4 = 1 : 3$) at 200 °C for 30 min, thermal annealing was performed at 1000 °C for 120 min in a 10% H_2 forming gas atmosphere to create NV centers and a hydrogen-terminated electroconductive surface. Next, the diamond was spin coated on the NV side with PMGI (Microchem, PMGI SF 6S) and ZEP-520A (ZEON, ZEP-520A) at 4000 rpm for 50 s with a slope of 10 s to form a double-layer resist

film with thicknesses of 220 nm and 200 nm respectively. The diamond was then baked at 225 °C for 5 minutes to harden the resist. After that, a regular array of nanoholes was patterned onto the resist film (diameter, 200 nm; spacing, 2 µm) through electron beam (EB) lithography. Thin Ti cylinders (diameter, 200 nm; thickness, 70 nm; spacing, 2 µm) were then fabricated on the diamond surface through EB vapor deposition and the resist was removed using a lift-off process. Finally, nanopillars were fabricated by inductively coupled plasma (ICP)-reactive ion etching (O_2, 30 SCCM, 1 Pa; ICP power, 700 W; Bias power 250 W) using the Ti cylinders as an etching mask. The diamond was cleaned again with hot-mixed acid ($HNO_3 : H_2SO_4 = 1 : 3$) at 200 °C for 30 min to remove the Ti mask. Thermal annealing was performed at 465 °C for 8 h in an O_2 gas atmosphere to create an oxygen-terminated surface and enhance the charge stability of shallow NV centers.

Pulsed ODMR measurements were performed using a home-built scanning confocal fluorescence microscopy (CFM) system. A schematic of our pulsed ODMR setup is shown in Fig. 2 (b). Our system is equipped with a 532 nm-laser (Changchun New Industries Optoelectronics Technology, MGL-III-532nm-300mW-1%), an acousto-optic modulator (Gooch & Housego, AOMO 3350-120), a piezo stage (PI, NanoCube P-611.3S) for objective scanning and a single-photon counting module (Laser Components, COUNT-100C). An air objective lens (Olympus, MPLAPON 50×) and a long-pass filter (≥650 nm) were used in all fluorescence measurements. Microwaves (MWs) at the resonant ODMR frequency (~2 GHz) were generated by a radio frequency (RF) analog signal generator (Keysight, E4428C) and pulsed by an RF circuit composed of a phase shifter, two switches and a combiner (Mini-Circuits, ZX10Q-2-25-S+, ZASWA-2-50DR+ and ZX10-2-442-S+). The MW pulses were amplified by a power amplifier (Mini-Circuits, ZHL-16W-43-S+) and applied to the NV center via a Cu wire antenna (diameter, 20 µm) placed on the diamond substrate surface. The RF switching was controlled by a data timing generator (Textronics, DTG5274). An Nd magnet supplied a static magnetic field (~30 mT), which was used to configure a two-level quantum system consisting of NV center electron spin $M_s = 0$ and $M_s = -1$ sublevels. The photon counting protocol was realized on a field-programmable gate array (FPGA) board (Digilent, Cora Z7-10) where a laboratory-designed hardware is implemented in hardware description language (HDL) code. The data acquired by the FPGA was processed using the Qudi software.[40] Qdyne measurements were performed in intervals of 23.516 µs, equivalent to the duration of an XY8-8 pulse sequence and some additional extra time.

Radio waves at 2 MHz were generated by an RF analog signal generator (Keysight, N5181A), amplified by a power amplifier (Mini-Circuits, LZY-22+) and applied to the NV center using a hand-wound coil (coil diameter, ~38 mm; wire diameter, 0.40 mm; coil turns, 50) surrounding the diamond substrate.

A scanning electron microscope (SEM) image of a fabricated nanopillar is shown in Fig. 2 (c). The image is taken after removing the Ti mask. We note that the charge-up effect is quite severe when procuring this image, even after surface termination with hydrogen to create an electroconductive surface. Nevertheless, we are able to determine the diameter of the top facet, base and the pillar's height to be 93 nm, 261 nm and 260 nm respectively. The simple shape of the nanopillars makes them highly reproducible in mass production. In a regular array of nanopillars, all nanopillars exhibit a tapered shape with a flat top surface. The top and bottom diameters showed a standard deviation of 8.6 nm and 7.2 nm, while the height showed a standard deviation of 4.4 nm.

The depth profile of NV centers created by ^{15}N ion implantation at 2.5 keV was reported to range from 2 nm to 11 nm with approximately 50% of the NV centers located at a depth between 2 nm to 4 nm.[16] It was observed that the Ti cylinders used as pillar masks were not damaged by ICP-reactive ion etching, so we expect the NV centers beneath the cap to be unaffected during etching. The NV center production yield and number of NV centers per pillar was evaluated by previously reported methods.[16] It has been shown by Fukuda et al. through anti-bunching experiments that NV centers produced by our method are distributed about the diamond surface following a Poisson distribution characterized by the average number of NV centers per unit area, λ. In our case, the NV center fabrication yield was found to be 5.91%, which results in $\lambda = 0.589$. Note that this yield is significantly higher than that achieved by other implantation techniques, which typically have yields of less than 1%.[16] Furthermore, an empirical count of NV centers per nanopillar was obtained to verify our method for identifying nanopillars containing single NV centers. Single NV centers are identified by a characteristic ODMR dip of approximately 15%. Using this method, we counted the number of NV centers in each nanopillar and compare our results to the theoretically obtained Poisson distribution. The comparison of our empirical counts with the Poisson distribution is provided in Fig. 3. As can be seen in Fig. 3, approximately 30% of our nanopillars contain single NV centers and our empirically obtained NV center counts agrees closely with the theoretical distribution, with a sum of squared errors of 3.8×10^{-3}. Thus, we can successfully identify nanopillars with single NV centers. Using this process,

we choose only a nanopillar with a single NV center to conduct our measurements.

CFM images comparing the fluorescence profile of a shallow single NV center obtained from a nanopillar and unstructured flat diamond are shown in Fig. 4 (a) and (b) respectively. Visually, it can be seen from Fig. 4 that the single NV center in the nanopillar is much brighter than in flat diamond, while maintaining a similar dispersion profile. The average photon count detected from the nanopillar was measured to be 180 kC/s, while flat diamond only achieved 90 kC/s. The background fluorescence of the nanopillar and flat diamond were measured to be 40 kC/s and 50 kC/s respectively. Correcting for the background fluorescence, the fluorescence contribution of the single NV center in nanopillar and flat diamond are 140 kC/s and 40 kC/s respectively. Thus, the photon collection rate of the NV center in the nanopillar is 3.5 times higher than that in flat diamond and our requirement that photon counts must be consistently greater than 100 kC/s is satisfied.

Hahn echo measurements were performed to compare the electron spin coherence times T_2 of an NV center in a nanopillar after oxygen termination to that in flat diamond. The measured T_2 of a single NV center electron spin in a nanopillar is $5.7\,\mu s$, which is comparable to that in flat diamond at $4.5\,\mu s$. This coherence time has been proven to fulfill the requirement for detection of ^1H and ^{19}F spins placed on the diamond surface.[16] This result confirms that the charge characteristics of shallow single NV centers in oxygen-terminated nanopillars satisfies the requirements for nano-NMR measurements.

To test the effectiveness of a single NV center in an oxygen-terminated nanopillar for nano-NMR, qdyne measurements were performed. Each measurement was performed for $600\,s$, resulting in approximately 2.55×10^7 samples. The goal of the measurement is to detect an AMF with a frequency of $2\,MHz$, supplied by an RF analog signal generator. The power of the AMF applied to the NV center is estimated to be $6.10\,\mu T$, calculated from the current flowing through the coil. The spectra obtained using a single NV center in a nanopillar and flat diamond are shown in Fig. 5 (a) and (b) respectively. In each of the figures, simulated theoretical spectra are also shown. As can be seen from the spectra, there is a small discrepancy between the measured peak frequency and the original AMF frequency, which may be caused by a discrepancy between the clock of the RF analog signal generator and the data timing generator. It can also be seen from Fig. 5 that the enhanced photon collection from the nanopillar directly contributes to obtaining a clear spectral peak. The experimentally obtained

peak amplitude obtained with the nanopillar is 0.368, more than double that of the flat diamond at 0.178. Meanwhile, the floor level fluctuation (standard deviation from the averaged baseline) obtained with the nanopillar is 0.0417 and that of the flat diamond is 0.0406, which is a negligibly small difference. The simulated ideal frequency spectra were obtained through Monte Carlo simulations. The number of photons detected at each sampling point were drawn from a Poisson distribution parameterized by the photon collection rate and AMF frequency. As can be seen in Fig. 5, there is a 64% deviation between the simulated and measured peak amplitude of the nanopillar spectrum and a 36% deviation for the flat diamond spectrum. These deviations were confirmed to be owing mainly to the thermal drift of the laser optics and partially to background fluorescence and stray light.

In conclusion, we have presented a nanopillar design in the context of nano-NMR sensing with an NV center placed within $\mathbf{5\,nm}$ of the top facet. We have provided a simple fabrication procedure that yields highly reproducible nanopillars, suitable for mass production. With our fabricated nanopillars, we have shown a 3.5 times improvement in photon collection from the nanopillar resulting in an average photon count of 140 kC/s from a single NV center, which satisfies our requirement for tractable nano-NMR measurements. We have also shown that the single NV in our fabricated nanopillars have sufficiently long T_2 for nano-NMR measurements. Finally, we have demonstrated the effectiveness of our nanopillars in nano-NMR measurements by obtaining a 2 times improvement in the peak amplitude obtained through qdyne AMF measurements, with no significant increase in baseline fluctuations. With these demonstrations, we have effectively merged the developments in quantum sensing protocols with the developments in nano-photonic structures.

While these are large improvements over NV sensing performance in flat diamond, there is still a considerable discrepancy between our measured enhancement and the theoretical value calculated through simulations. We believe some major sources of these discrepancies to be sub-optimal nanopillar shape, as an artifact of the etching process, as well as laser optics thermal drift and background fluorescence effects. In future works, we will continue to improve our fabrication process, optical setup and measurement protocol to control these sources of error. Furthermore, the T_2 of shallow single NV centers in nanopillars are still too short to detect many nuclear species of interest. Increasing these T_2 times remain an avenue of future research.

Acknowledgment

This work was supported by Japan Society for the Promotion of Science (JSPS) KAKENHI Grant Number JP22H01921, JP18H03766 and JP23H00169, and partly by Advanced Research Infrastructure for Materials and Nanotechnology in Japan (ARIM) and Design & Engineering by Joint Inverse Innovation for Materials Architecture (DEJI^{2}MA) of the Ministry of Education, Culture, Sports, Science and Technology (MEXT). We also acknowledge the support of MEXT Q-LEAP (JPMXS0118068379), JST CREST (JPMJCR1773), JST Moonshot R&D (JPMJMS2062), MIC R&D for construction of a global quantum cryptography network (JPMI00316), JSPS KAKENHI (No. 20H02187 and 20H05661).

References

1) J. R. Maze, P. L. Stanwix, J. S. Hodges, S. Hong, J. M. Taylor, P. Cappellaro, L. Jiang, M. V. Gurudev Dutt, E. Togan, A. S. Zibrov, A. Yacoby, R. L. Walsworth, and M. D. Lukin, Nature 455 644 (2008).
2) V. S. Perunicic, L. T. Hall, D. A. Simpson, C. D. Hill, and L. C. L. Hollenberg, Phys. Rev. B 89 054432 (2014).
3) L. M. Pham, S. J. DeVience, F. Casola, I. Lovchinsky, A. O. Sushkov, E. Bersin, J. Lee, E. Urbach, P. Cappellaro, H. Park, A. Yacoby, M. Lukin, and R. L. Walsworth, Phys. Rev. B 93 045425 (2016).
4) R. Schirhagl, K. Chang, M. Loretz, C. L. Degen, Annu. Rev. Phys. Chem. 65 83-105 (2014).
5) N, Aharon, I. Schwartz, and A, Retzker, Phys. Rev. Lett. 122 120403 (2019).
6) G. Balasubramanian, P. Neumann, D. Twitchen, M. Markham, R. Kolesov, N. Mizuochi, J. Isoya, J. Achard, J. Beck, J. Tissler, V. Jacques, P. R. Hemmer, F. Jelezko, and J. Wrachtrup, Nat. Mat. 8 383 (2009).
7) T. Yamamoto, C. Müller, L. P. McGuiness, T. Teraji, B. Naydenov, S. Onoda, T. Ohshima, J. Wrachtrup, F. Jelezko, and J. Isoya, Phys. Rev. B 88 201201 (2013).
8) A. Gruber, A. Dräbenstedrat, C. Tietz, L. Fleury, J. Wrachtrup, and C. von Borczyskowski, Science 276 2012 (1997).
9) F. Jelezko, T. Gaebel, I. Popa, A. Gruber, and J. Wrachtrup, Phys. Rev. Lett. 92 076401 (2004).
10) F. Alghannam, P. Hammer, Sci. Rep. 9 5870 (2019).
11) I. Lovchinsky, A. O. Sushkov, E. Urbach, N. P. de Leon, S. Choi, K. De Greve, R. Evans, R. Gertner, E. Bersin, C. Müller, L. McGuinness, F. Jelezko, R. L. Walsworth, H. Park and M. D. Lukin, Science. 351, 836 (2016).
12) N. Aslam, M. Pfender, P. Neumann, R. Reuter, A. Zappe, F. F. de Oliveira, A. Denisenko, H. Sumiya, S. Onoda, J. Isoya, and J. Wrachtrup, Science 357 67 (2017).
13) D. R. Glenn, D. B. Bucher, J. Lee, M. D. Lukin, H. Park, and R. L. Walsworth, Nature 555 351 (2018).
14) Y. Romach, C. Müller, T. Unden, L. J. Rogers, T. Isoda, K. M. Itoh, M. Markham, A. Stacey, J. Meijer, S. Pezzagna, B. Naydenov, L. P. McGuinness,

N. Bar-Gill, F. Jelezko, Phys. Rev. Lett. 114 017601 (2015).
15) B. A. Myers, M. C. Dartiailh, K. Ohno, D. D. Awschalom, A. C. Bleszynski Jayich, Phys. Rev. Lett. 113 027602 (2014).
16) R. Fukuda, P. Balasubramanian, I. Higashimata, G. Koike, T. Okada, R. Kagami, T. Teraji, S. Onoda, M. Haruyama, K. Yamada, M. Inaba, H. Yamano, F. M. Stürner, S. Schmitt, L. P. McGuinness, F. Jelezko, T. Ohshima, T. Shinada, H. Kawarada, W. Kada, O. Hanaizumi, T. Tanii, J. Isoya, New J. Phys. 20 083029 (2018).
17) S. Schmitt, T. Gefen, F. M. Stürner, T. Unden, G. Wolff, C. Müller, J. Scheuer, B. Naydenov, M. Markham, S. Pezzagna, J. Meijer, I. Schwarz, M. Plenio, A. Retzker, L. P. McGuinness, and F. Jelezko, Science 356 832-837 (2017).
18) I. Schwartz, J. Rosskopf, S. Schmitt, B. Tratzmiller, Q. Chen, L. P. McGuinness, F. Jelezko, and M. B. Plenio, Sci. Rep. 9 6938 (2019).
19) J. M. Boss, K. S. Cujia, J. Zopes, and C. L. Degen, Science 356 837–840 (2017).
20) G. A .Álvarez, and D. Suter, Phys. Rev. Lett. 107 230501 (2017).
21) M. Celebrano, M. Baselli, M. Bollani, J. Frigerio, A. B. Shehat, A. D. Frera, A. Tosi, A. Farina, F. Pezzoli, J. Osmond, X. Wu, B. Hecht, R. Sordan, D. Chrastina, G. Isella, L. Duò, M. Finazzi, and P. Biagioni, ACS Photonics 2 1 53-59 (2015).
22) B. J. M. Hausmann, T. M. Babinec, J. T. Choy, J. S. Hodges, S. Hong, I. Bulu, A. Yacoby, M. D. Lukin and M. Lonv̈car, New J. Phys. 13 045004 (2011).
23) P. Maletinsky, S. Hong, M. S. Grinolds, B. Hausmann, M. D. Lukin, R. L. Walsworth, M. Loncar, and A. Yacoby, Nat. Nanotechnol. 7 320–324 (2012).
24) M. S. Grinolds, S. Hong, P. Maletinsky, L. Luan, M. D. Lukin, R. L. Walsworth, and A. Yacoby, Nat. Phys. 9 215–219 (2013).
25) L. Luan, M. S. Grinolds, S. Hong, P. Maletinsky, R. L. Walsworth, and A. Yacoby, Sci. Rep. 5 8119 (2015).
26) S. Furuyama, K. Tahara, T. Iwasaki, M. Shimizu, J. Yaita, M. Kondo, T. Kodera, and M. Hatano, Appl. Phys. Lett. 107 163102 (2015).
27) P. Appel, M. Ganzhorn, E. Neu, and P. Maletinsky, New J. Phys. 17 112001 (2015).
28) L. Thiel, D. Rohner, M. Ganzhorn, P. Appel, E. Neu, B. Müller, R. Kleiner, D. Koelle, and P. Maletinsky, Nat. Nanotechnol. 11 677–681 (2016).
29) M. Pelliccione, A. Jenkins, P. Ovartchaiyapong, C. Reetz, E. Emmanouilidou,

N. Ni, and A. C. B. Jayich, Nat. Nanotechnol. 11 700–705 (2016).
30) T. X. Zhou, R. J. Stöhr, and A. Yacoby, Appl. Phys. Lett. 111 163106 (2017).
31) A. Ariyaratne, D. Bluvstein, B. A. Myers, and A. C. B. Jayich, Nat. Commun. 9 2406 (2018).
32) L. Xie, T. X. Zhou, R. J. Stöhr, and A. Yacoby, Adv. Mater. 30 11 1705501(2018).
33) D. J. McCloskey, N. Dontschuk, D. A. Broadway, A. Nadarajah, A. Stacey, J. P. Tetienne, L. C. L. Hollenberg, S. Prawer, and D. A. Simpson, ACS Appl. Mater. Interfaces 12 11 13421–13427 (2020).
34) J. Kleinlein, T. Borzenko, F. Münzhuber, J. Brehm, T. Kiessling, and L. W. Molenkamp, Microelectron. Eng. 159 70–74 (2016).
35) B. J. M. Hausmann, M. Khan, Y. Zhang, T. M. Babinec, K. Martinick, M. McCutcheon, P. R. Hemmer, and M. Lončar, Diam. Relat. Mat. 19 621–629 (2010).
36) S. A. Momenzadeh, R. J. Stöhr, F. F. D. Oliveira, A. Brunner, A. Denisenko, S. Yang, F. Reinhard, and J. Wrachtrup, Nano Lett. 15 1 165–169 (2015).
37) K. Volkova, J. Heupel, S. Trofimov, F. Betz, R. Colom, R. W. MacQueen, S. Akhundzada, M. Reginka, A. Ehresmann, J. P. Reithmaier, S. Burger, C. Popov, and B. Naydenov, Nanomaterials 12 9 1516 (2022).
38) T. Teraji, T. Yamamoto, K. Watanabe, Y. Koide, J. Isoya, S. Onoda, T. Ohshima, L. J. Rogers, F. Jelezko, P. Neumann, J. Wrachtrup, and S. Koizumi, Phys. Status. Solidi. A 212 11 2365-2384 (2015).
39) T. Teraji, J. Appl. Phys. 118 115304 (2015).
40) J. M. Binder, A. Stark, N. Tomek, J. Scheuer, F. Frank, K. D. Jahnke, C. Müller, S. Schmitt, M. H. Metsch, T. Unden, T. Gehring, A. Huck, U. L. Andersen, L. J. Rogers, and F. Jelezko, SoftwareX 6 85-90 (2017).

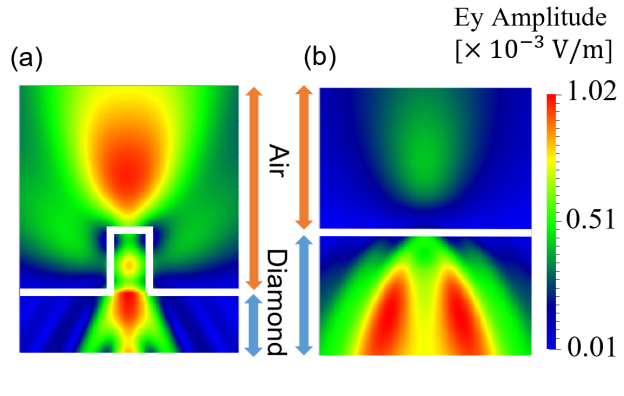

Fig. 1. FDTD simulations showing the side fluorescence profile of a shallow single NV center in (a) a diamond nanopillar and (b) unstructured flat diamond.

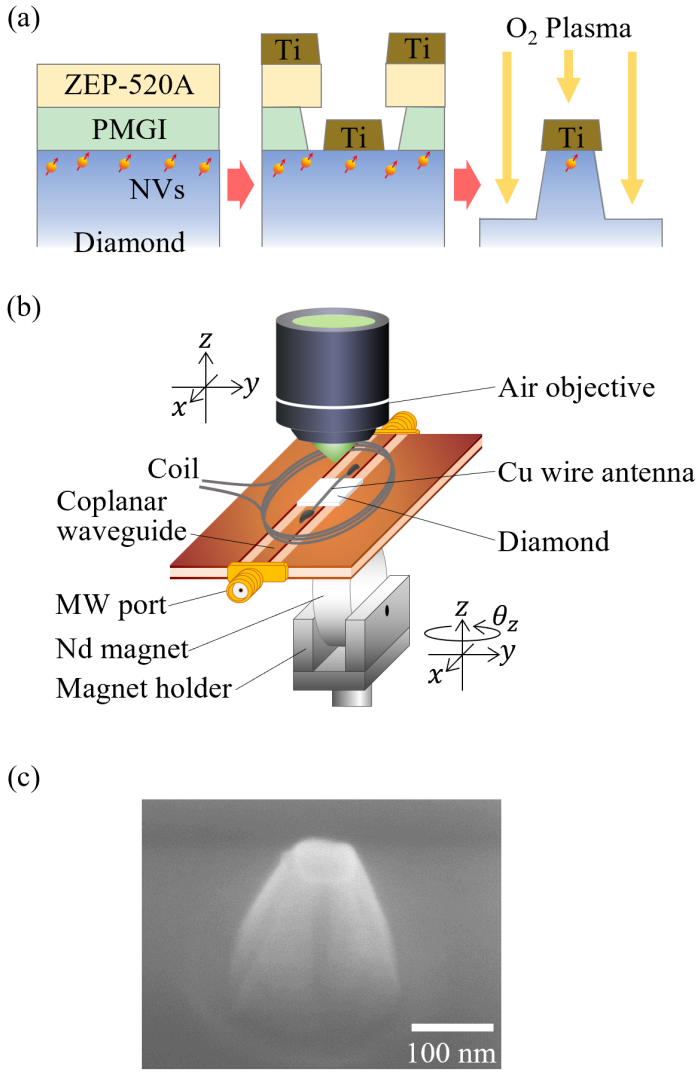

Fig. 2. (a) Schematic of the nanopillar fabrication process. (left) A double layer resist film is spin-coated after creating shallow NV centers in the diamond. (center) Titanium is deposited after the double layer resist film was patterned. (right) A nanopillar is fabricated by O_2-plasma etching. (b) Sample setup for the pulsed ODMR measurements. (c) SEM image (bird's eye view) of a nanopillar after the Ti mask was removed by hot mixed acid cleaning.

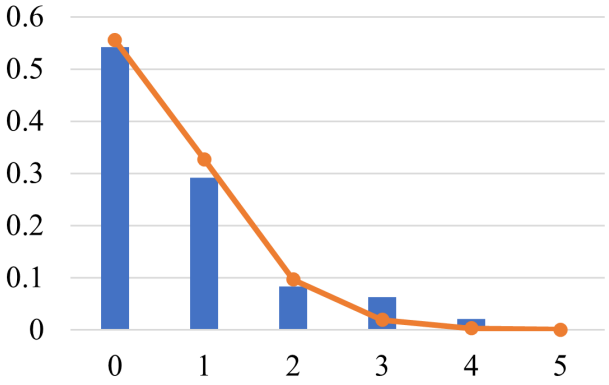

Fig. 3. Comparison between theoretical NV center Poisson distribution (orange line) with empirically counted number of NV centers (blue bars).

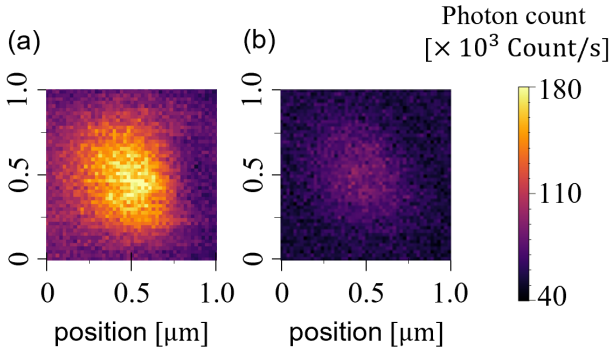

Fig. 4. CFM images showing the top fluorescence profile of a shallow single NV center in (a) a diamond nanopillar and (b) unstructured flat diamond.

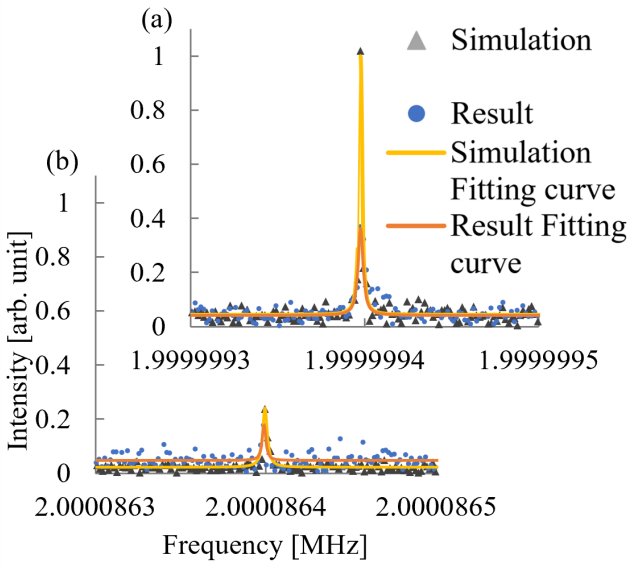

Fig. 5. Frequency spectrum obtained by qdyne measurements and simulation for a shallow single NV center in (a) a diamond nanopillar and (b) unstructured flat diamond.